Journal of Materials Chemistry A

ROYAL SOCIETY OF CHEMISTRY

COMMUNICATION

View Article Online
View Journal

Cite this: DOI: 10.1039/d2ta02339c

Li alloy anodes for high-rate and high-areal-capacity solid-state batteries†

Yonglin Huang, Bowen Shao and Fudong Han *

Received 23rd March 2022
Accepted 27th May 2022

DOI: 10.1039/d2ta02339c

rsc.li/materials-a

The serious challenges in utilizing Li metal anodes with solid electrolytes (SEs) have stimulated the research on developing alternative anodes for solid-state batteries (SSBs). Alloy-based anodes in SSBs have been gaining great interest recently due to their high capacities. Compared with Li metal, the slightly higher voltages of alloy anodes can help to improve the interfacial stability with SEs, but using alloy anodes cannot perfectly prevent the dendrite formation. Besides, a detailed understanding of the dendrite suppression capability of alloy anodes is still missing. Here we aim to provide some insights by evaluating the dendrite suppression capability of common Li alloys, including Li–Zn, Li–Si, Li–Sn, and Li–Al. It is found that even for alloy anodes with medium lithium contents and a three-dimensional alloy/SE composite structure, soft shorting of SSBs still occurred for some alloys. Among all the alloy anodes studied in this work, Li–Al exhibited the highest capability of suppressing dendrite formation. No soft shorting can be observed when symmetric cells using Li–Al anodes were tested at a high current density of 40 mA cm^{-2} with a capacity of 3 mA h cm^{-2}. The excellent dendrite suppression capability of Li–Al alloy was also demonstrated in solid-state lithium–sulfur batteries with a high cathode loading of 10 mA h cm^{-2}. The results indicate that Li–Al alloy can be used as a promising anode for high-rate and high-areal-capacity SSBs. The differences in the dendrite suppression of various alloys also imply that the mechanical properties of alloys may play a very important role in governing dendrite formation on these anodes.

1 Introduction

Solid electrolytes (SEs) are considered as the "enabler" of high-energy Li metal anodes.[1,2] However, successful utilization of Li metal in solid-state batteries (SSBs) has proven difficult due to (i) poor contact and (electro)chemical instability between Li metal and SEs,[3–5] (ii) dendrite penetration through SEs,[6–9] and (iii) morphological instability of Li metal.[10–13] Intimate interfacial contact can be achieved for many Li-SE combinations through the formation of interphases (chemical wetting)[14] or the application of stacking pressure,[12,15] and the charge-transfer kinetics of Li/SE interfaces (even with the presence of interphases) for some SEs has been demonstrated to be very fast.[16,17] However, plating Li at a high current density is very challenging due to dendrite penetration through SEs, by mechanisms that remain elusive.[18] Another key challenge of using Li metal is its morphological instability. Due to the self-diffusion limitation in Li metal itself, voids can be formed at Li/SE interfaces during stripping even with a large stacking pressure.[11] These voids may lead to contact loss and thus promote dendrite formation during the subsequent plating process.[12,19] The accumulation of voids inside Li metal will also alter the volume and the mechanical properties of the bulk anodes, complicating the strain/stress control in solid-state Li metal batteries. While continuous efforts are certainly needed to address these challenges, it is also imperative to explore alternative anodes for SSBs.

It should be noted that significant effort has been made to apply Ge,[20] Al,[21,22] Sn,[23] Au,[24,25] Si,[26] Mg,[27] and Ag[28] as the interlayers between Li metal and SEs. The alloy interlayers have led to a decrease in the interfacial resistance for as-assembled SSBs due to the enhanced wettability with SEs. However, the long-term effectiveness of alloy interlayers is questionable given the difficulties of maintaining the interlayers at the interfaces.[29] The current density and the areal capacity for Li cycling in those interface-engineered anodes are still limited. As a result, there is growing interest in using alloys as anodes for SSBs, *i.e.*, using alloying/dealloying instead of plating/stripping processes for lithium storage.[30–39] Alloy anodes, such as Si, Sn, and Al, have been widely studied in conventional lithium-ion batteries.[40] Even though alloy anodes have lower capacities and slightly higher voltages than Li metal anodes, the energy density, especially the volumetric energy density, of SSBs using alloy

Department of Mechanical, Aerospace and Nuclear Engineering, Rensselaer Polytechnic Institute, 110 8th Street, Troy, New York 12180, USA. E-mail: hanf2@rpi.edu

† Electronic supplementary information (ESI) available. See https://doi.org/10.1039/d2ta02339c

anodes can be comparable to or higher than that of conventional lithium-ion batteries.[41] The slightly higher voltage can effectively alleviate the electrochemical decomposition of SEs. The improvement of the interfacial stability between alloy anodes (Li–Al, Li–Sn, and Li–Si) and thiophosphate SEs has also been observed in previous works.[42–44] Li–In alloy with a stable voltage plateau of around 0.6 V has been widely used as the counter and reference electrodes in lab-scale SSBs to evaluate the performance of electrodes and SEs.[35,45] Nevertheless, the low capacity (113 mA h g^{-1} for $Li_{0.5}In$) and high cost of indium limit its further application in practical cells. Future SSBs will require alloy anodes with high capacities and low cost. Furthermore, due to the limited chemical diffusion of lithium in the alloy, the direct Li plating on the alloy anode may occur even if the overall composition of the alloy anode is still within the range of alloy phases, especially under high current density where a large overpotential is present.[11] This continuous Li plating may lead to penetration of Li dendrites inside SEs, causing short-circuiting. However, the dendrite suppression capability of these alloy anodes in SSBs has rarely been studied.

Several factors should be considered to prevent dendrite formation in alloy-based SSBs. The first one would be the electrode potential which is related to both the thermodynamics and kinetics of the electrode. If the equilibrium potential of the alloy is low and the overpotential during Li alloying is high, the real voltage of the alloy anode can be lower than the Li-plating potential, thus enabling dendrite formation. Another factor is related to the morphological instability of alloy anodes. Although lithium diffuses faster in some alloys (*e.g.*, Li–Mg and Li–Al) than in pure Li metal,[11,46] the different diffusion coefficients in the alloys can cause the change of the morphological instability of alloy anodes,[44] which in turn leads to variations in the interfacial contact and the dendrite suppression capability. In addition, the large volume change of anode active materials also poses significant challenges to maintaining the interfacial contact between alloy anodes and SEs. In this regard, the mechanical properties of the alloys will play an important role, considering that a large stacking pressure is usually applied during the cycling of SSBs.[12,15,41,47] While tremendous efforts have been devoted to developing alloy anodes for conventional liquid-electrolyte lithium-ion batteries, the design principles of alloy anodes in SSBs can be quite different due to the distinct differences between SEs and liquid electrolytes.[48] Understanding the dominating factor for dendrite formation on alloy anodes is important for developing feasible alloy anodes in SSBs, but this important knowledge is still missing.

In this work, we aim to provide some insights into the dendrite formation in alloy-based SSBs based on the evaluation of the dendrite suppression capability of common Li alloys, including Li–Zn, Li–Si, Li–Sn, and Li–Al. Alloys with very low voltage (*e.g.*, ~0.03 V for Li–Mg[40,49]) are prone to Li plating and are therefore not included in this study. Li alloys with medium lithium contents, corresponding to a moderate voltage range for each alloy, were used in this study. The alloys were powdered, sieved to similar particle sizes, and mixed with SEs to make composite anodes with a fixed volume fraction of the alloys.[50,51] The idea is that if dendrites are formed in the three-dimensional (3D) alloy composites, they would be more easily formed when using two-dimensional alloy discs with high lithium contents as anodes, and therefore the results from this study are close to the upper limit of the dendrite suppression capability of these alloys. We report that Li–Al alloy composites exhibited the best performance in terms of dendrite suppression and highlight the important role of the mechanical properties of the alloys in governing dendrite formation in alloy-based SSBs. We further demonstrated the application of Li–Al alloy composites in high-current-density and high-areal-capacity solid-state lithium–sulfur batteries.

2 Results and discussion

2.1 Alloy composition, synthesis, and characterization

Li alloys with medium lithium contents were used in this work. The lithium content of each Li alloy is neither too high to induce Li plating, nor too low to avoid limited lithium amount and high alloy voltage. The compositions of the alloys are also shown in the phase diagrams (Fig. S1†). The utilization of Li alloys can be evaluated electrochemically by using symmetric cells. The study will further provide important information on the performance of alloy anodes for their application with non-lithium-containing cathodes, such as sulfur or conversion-type

Table 1 Composition, equilibrium potential, and specific capacity of the alloys used in this work

Alloy	Composition	Equilibrium potential (V *vs.* Li/Li^+)	Specific capacity (mA h g^{-1})
Li–Zn	$LiZn_2$	0.26	196
Li–Si	Li_2Si	0.50	1276
Li–Sn	Li_7Sn_3	0.53	463
Li–Al	Li_4Al_6	0.37	564

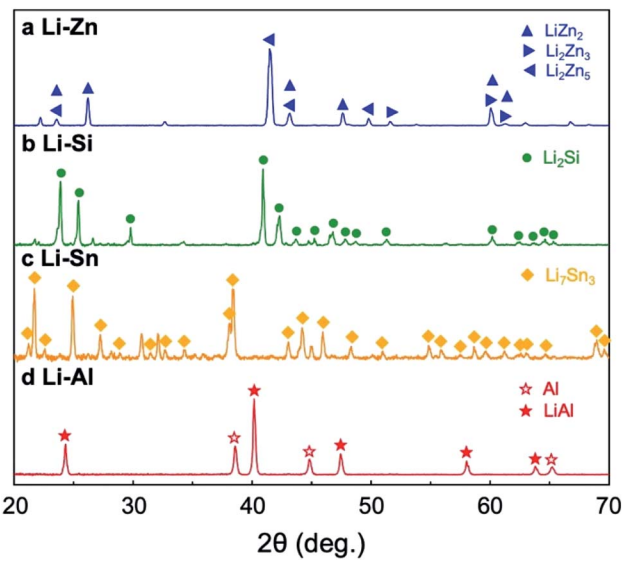

Fig. 1 XRD patterns of the Li–Zn (a), Li–Si (b), Li–Sn (c), and Li–Al (d) alloys.

materials. Table 1 summarizes the composition, equilibrium potential,[43,52–54] and specific capacity of $LiZn_2$, Li_2Si, Li_7Sn_3, and Li_4Al_6. The compositions of the alloys are identified in the moderate-voltage range while having fairly high capacities. These alloys were prepared by the direct alloying process. Li and alloying components with specific stoichiometric ratios were heated above their liquidus temperature and cooled down to room temperature. No impurities can be observed from the XRD patterns of these as-synthesized alloys (Fig. 1). Single phases Li_7Sn_3 and Li_2Si are formed, and composite phases are formed for Li_4Al_6 (Al and LiAl phases) and $LiZn_2$ ($LiZn_2$, Li_2Zn_3, and Li_2Zn_5 phases), consistent with the phase diagrams of these alloys.[55] The alloys were pulverized and sieved through a 50 μm sieve, leading to alloy powders with similar particle sizes, although the size of Li–Zn is slightly larger than the other alloys (Fig. S2†). The alloy powders were then mixed with SE $Li_{5.4}PS_{4.4}Cl_{1.6}$ (LPSCl, Fig. S3†) to form 3D composite anodes. To compare the electrochemical performance of different alloys, the volume fractions of the alloys in the composite anodes are kept at 50% and the total capacities of the composite anodes in each symmetrical cell are around 30 mA h.

2.2 Li cycling of alloy anodes in symmetric cells

To investigate the dendrite suppression capability of various alloy anodes, we first evaluate the cycling performance of Li alloys in alloy|LPSCl|alloy symmetric cells. These alloys demonstrated excellent interfacial stability with the SE (Fig. S4†), indicating that the utilization of alloy anodes with a higher electrode potential than Li metal can effectively suppress the SE decomposition. The cells were tested with increasing current density. The capacity at each current is 3 mA h cm^{-2}, and the total capacity provided by each composite anode is around 30 mA h. The voltage profiles of the symmetric cells are shown in Fig. 2. Sloping voltage profiles can be observed for the alloys due to the multiple phase transitions

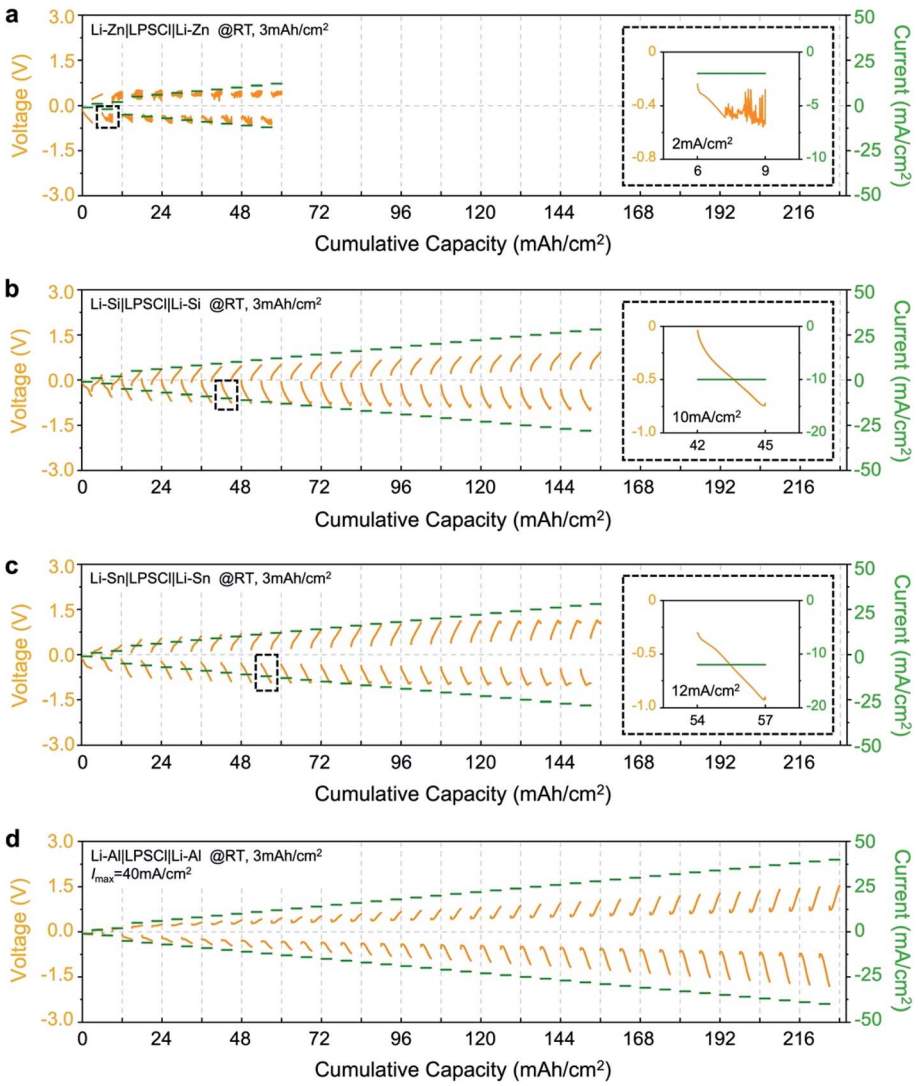

Fig. 2 Voltage and current profiles of Li–Zn (a), Li–Si (b), Li–Sn (c), and Li–Al (d) anodes as a function of cumulative capacity in symmetric cells. The capacity is 3 mA h cm^{-2} per charge and discharge process. The insets in (a), (b), and (c) show the voltage curves and corresponding current densities for the initial soft shorting of the cells. All cells were tested at room temperature.

and electrode kinetics. At low currents, the voltage gradually increases with the current. However, at a certain current, the voltage of some cells will decrease, occasionally with some voltage fluctuations, as shown in the insets of Fig. 2a–c. This voltage decrease is considered a result of soft shorting due to dendrite formation in the SE.[56,57] The soft-shorting of the cell is also confirmed by the fact that the voltage of the cell does not increase obviously with the current at large cumulative capacities (>12 mA h cm^{-2} for Li–Zn, >48 mA h cm^{-2} for Li–Si, and >60 mA h cm^{-2} for Li–Sn). Fig. 2a shows that for the Li–Zn anode, soft shorting occurs at a current density of 2 mA cm^{-2}. Soft shorting is also observed for Li–Si and Li–Sn anodes at current densities of 10 mA cm^{-2} (Fig. 2b) and 12 mA cm^{-2} (Fig. 2c), respectively. Although these maximum current densities are much higher than that of the composite anodes composed of Li metal powders and LPSCl (0.5 mA cm^{-2} at 0.25 mA h cm^{-2}, Fig. S5†), the results indicate that the utilization of alloy anodes cannot completely prevent dendrite formation in SSBs. Remarkably, no soft shorting can be observed for Li–Al alloy as the current density increases to 40 mA cm^{-2}, even though the real voltage of the Li–Al anode may be already much lower than 0 V *vs.* Li/Li^+ due to the large overpotential of Li–Al anode at higher current densities.

To further confirm the excellent capability of suppressing dendrite formation on Li–Al alloy, we then evaluated the long-term cycling stability of Li–Al composite anodes in symmetric cells. Fig. 3a and b show the voltage profiles of Li–Al|LPSCl|Li–Al symmetric cells cycled at 5 mA cm^{-2} with a capacity of 3 mA h cm^{-2}. A very stable cycling performance can be observed. Even when cycled at an extremely high current density of 10 mA cm^{-2} (Fig. 3c and d), the symmetric cell can still operate for more than 100 cycles without any short-circuiting. The stable cycling of Li–Al alloy is also demonstrated in the cells with higher utilization of lithium in Li–Al composite anodes. As shown in Fig. S6,† at a higher utilization of 30%, no shorting can be observed from the Li–Al|LPSCl|Li–In cell at 5 mA cm^{-2}, and this cell can be stably cycled at 2 mA cm^{-2} for at least 100 cycles. The results confirmed that Li–Al alloy can be used as a very promising anode material for high-current-density and high-areal-capacity SSBs.

2.3 Electrochemical performance of Li–Al anodes in solid-state lithium–sulfur batteries

The electrochemical performance of Li–Al alloy was also demonstrated in solid-state full cells with sulfur cathodes. The areal loading of the sulfur cathode is 10 mA h cm^{-2}. The areal loading of the Li–Al composite anode is fixed at 34 mA h cm^{-2}, which leads to the capacity ratio of negative to positive electrodes (N/P ratio) to be 3.4 : 1. It should be noted that overly excessive Li was commonly used in the anodes of both solid-state and liquid-electrolyte lithium–sulfur batteries due to the instability between Li and electrolytes. The lithium utilization in this work is the highest compared with previous efforts. The rate performance of solid-state lithium–sulfur batteries was tested at 25 °C (Fig. 4a and c) and 60 °C (Fig. 4b and d). The voltage plateau corresponding to inter-conversion between S and Li_2S can be observed from the voltage profiles at 25 °C (Fig. 4a) and 60 °C (Fig. 4b). The reversible charge capacity at room temperature is 1216, 1141, 1013, 680, 400, 240, and 145 mA h g^{-1} at 0.5, 1.0, 2.0, 4.0, 6.0, 8.0, and 10.0 mA cm^{-2}, respectively (Fig. 4c). As shown in Fig. 4b, testing the Li–Al|LPSCl|S cell at 60 °C helps improve the kinetics of the cell with a decreased voltage hysteresis and an increased capacity at each current density (Fig. 4b). The reversible charge capacity at different current densities is 1488, 1368, 1175, 836, 513, 307, and 189 mA h g^{-1} (Fig. 4d). The results indicate that the full cells can still operate without shorting and deliver impressive capacities at large currents. The long-term cycling stability at 2

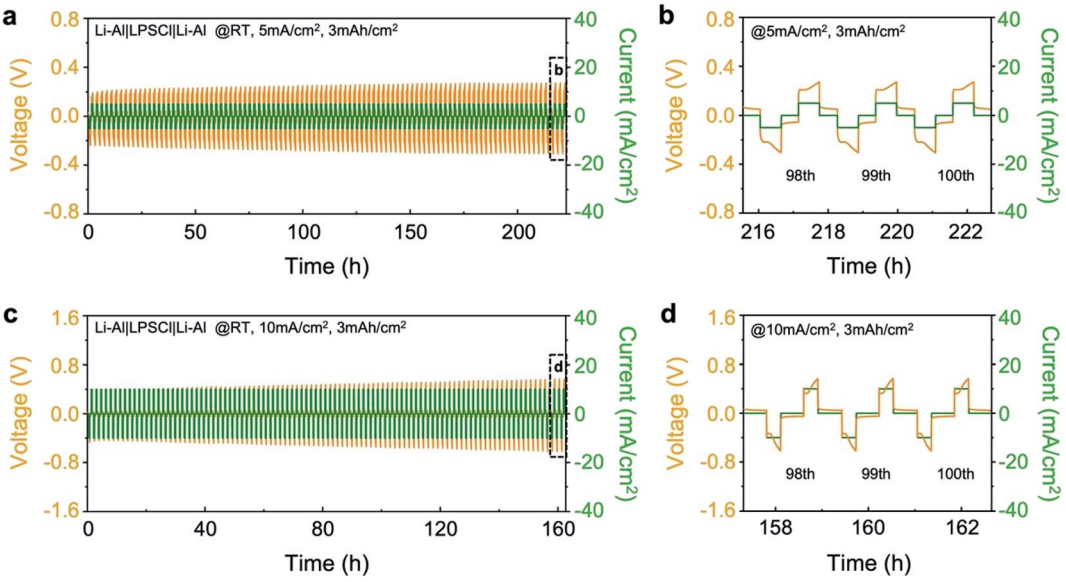

Fig. 3 The cycling performance of Li–Al|LPSCl|Li–Al symmetric cells at 5 mA cm^{-2} (a) and 10 mA cm^{-2} (c). The cycling capacity is 3 mA h cm^{-2}. (b) and (d) show three enlarged voltage curves from (a) and (c), respectively. The cells were tested at room temperature.

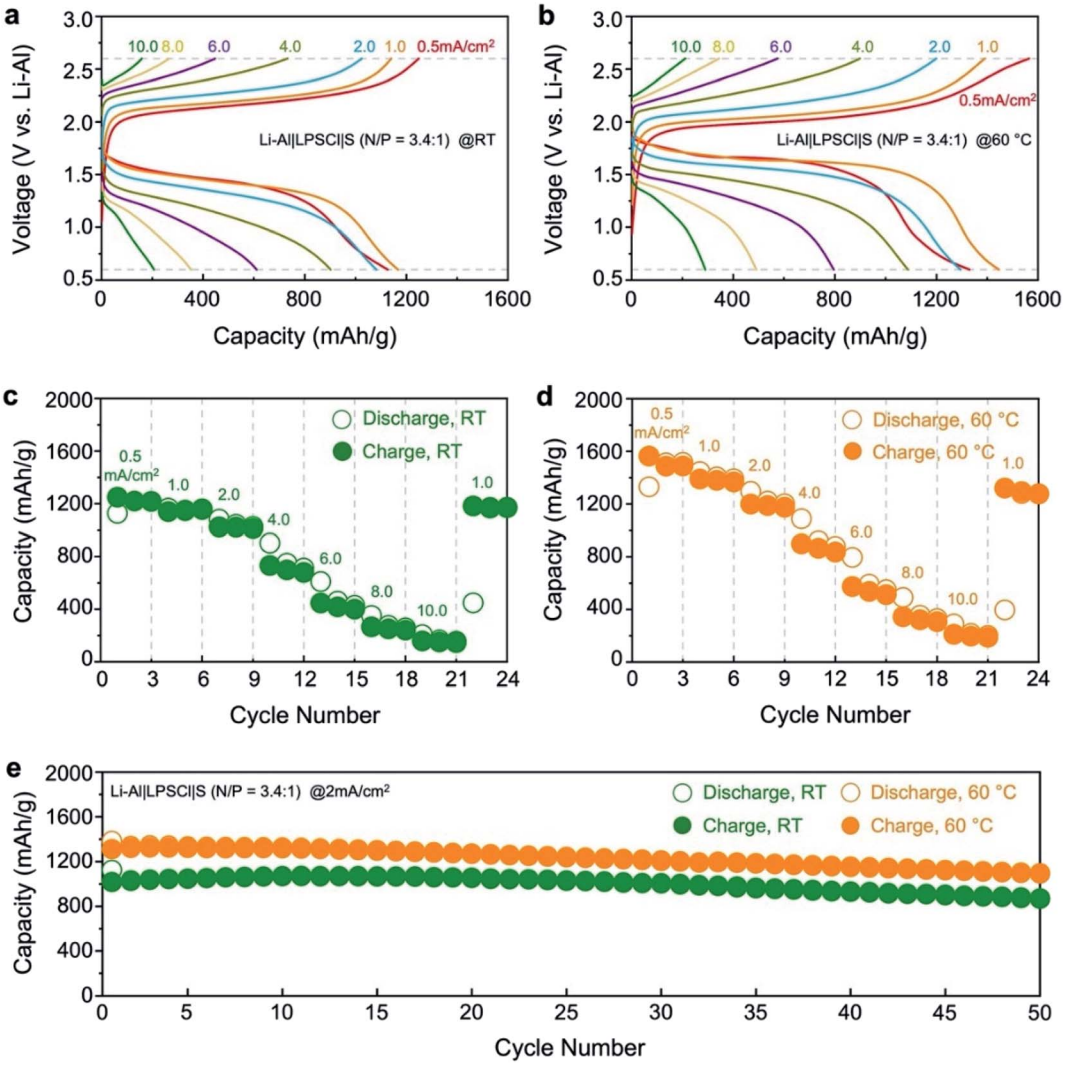

Fig. 4 Charge/discharge curves of Li–Al|LPSCl|S full cells at different current densities at 25 °C (a) and 60 °C (b). The rate performance of Li–Al|LPSCl|S full cells at 25 °C (c) and 60 °C (d). (e) Cycling performance of Li–Al|LPSCl|S full cells at 2 mA cm^{-2} (corresponding to 0.2C) at 60 °C.

mA cm^{-2} is also confirmed in Fig. 4e, as only a slight capacity decay can be observed in the first 50 cycles.

We then compare the performance of the anodes for solid-state lithium–sulfur batteries. Fig. 5 summarizes the current density and actual areal capacity of all reported solid-state lithium–sulfur batteries. Tables S1 and S2 in the ESI† provide detailed information for the data at ambient temperature and elevated temperature, respectively. It should be noted that the utilization of Li-containing anode active material has never been considered in previously reported solid-state lithium–sulfur batteries. Fig. 5 shows that even at a low utilization rate of Li, which is commonly used in previous research on solid-state lithium–sulfur batteries, the current density and the areal capacity of these batteries are limited. In this work, the current density and areal capacity of the Li–Al|LPSCl|S full cell with maximum lithium utilization are among the highest in all literature reports, regardless of the anode materials used for the full cells, highlighting the excellent performance of Li–Al alloy as the anode material for SSBs.

2.4 Discussion

The electrochemical performance of various Li alloys in this work indicates that the utilization of alloy anodes cannot prevent dendrite formation in SSBs, even if the lithium content in the alloy is not high and the alloy is mixed with SE to form a composite anode. The results also indicate that the Li–Al alloy outperforms the other Li alloys as a promising anode for high-current-density and high-areal-capacity SSBs. An important question would be what characteristics make Li–Al alloy such a great anode in terms of suppressing Li penetration in SEs. In Table 1, the equilibrium potential of Li–Al alloy is closer to 0 V *vs.* Li/Li^+ than those of Li–Si and Li–Sn. At a high current density (*e.g.*, 40 mA cm^{-2}), the overpotential of Li–Al can be much higher than the voltage at which soft shorting occurs in Li–Si and Li–Sn alloys (the insets of Fig. 2b and c). This information implies that the electrode potential of the alloy anode may not be the dominant factor for Li dendrites on the alloy. Considering that the lithium diffusion coefficient of Li–Al (10^{-9} cm^2

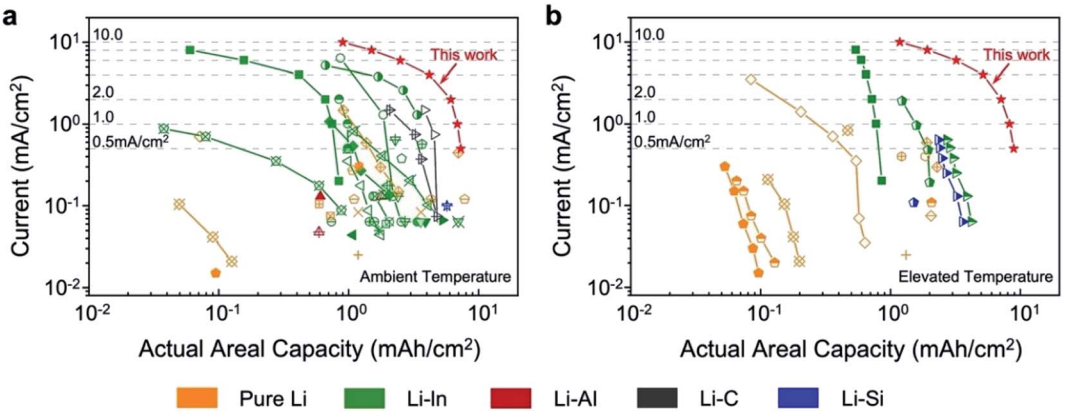

Fig. 5 Comparison of the current density and actual areal capacity of solid-state lithium–sulfur batteries with various Li-containing anodes. The data is presented in two plots based on their testing temperature: ambient temperature (20 to 30 °C) (a) and elevated temperature (40 to 80 °C) (b). Detailed information for each data is included in the ESI.†

s^{-1} in LiAl phase[58]) is comparable with that of Li–Zn (8.8×10^{-10} to 3.7×10^{-9} cm^2 s^{-1} in LiZn phase[59]) but is much smaller than that of Li–Sn (3×10^{-7} to 5×10^{-7} cm^2 s^{-1} in Li_7Sn_3 phase[59]), the lithium diffusion in Li alloy itself should not be considered as the primary factor either.

We, therefore, suspect that the superior dendrite suppression capability may be related to the excellent mechanical properties of Li–Al alloy. As a preliminary effort to test this hypothesis, we did the compression test of the four alloys studied in this work. To prepare the specimens for the compression test, powders of each alloy were pressed into a pellet with a diameter of 8 mm and a thickness of 2 mm under 1000 MPa. Fig. 6 compares the stress–strain curves of the alloys. Li–Al alloy shows the highest compressive strength among all the alloys. Besides, Li–Al, Li–Si, and Li–Sn are characterized by the yield behavior after the linear stress–strain region, while Li–Zn alloy is characterized by the absence of any appreciable change in strain rate before rupture occurs, suggesting the brittle feature of Li–Zn.[60] The result also shows that Li–Al alloy has a slightly higher Young's modulus than the other alloys. The excellent compressive strength and slightly higher Young's modulus of Li–Al can effectively maintain its integrity and the contact with SE during long-term cycling, *i.e.*, repeated loading and unloading, and thus improve the dendrite suppression capability. Although Li–Sn and Li–Si alloys exhibit lower compressive strength than Li–Zn alloy, the lower specific capacity (corresponding to a thicker composite electrode for lithium to diffuse through), lower electrode potential, and lower lithium diffusion coefficient of Li–Zn alloy may lead to its poor dendrite suppression capability when compared with Li–Sn and Li–Si. Therefore, the dendrite suppression capability of an alloy anode is a combined effect of multiple reasons and the mechanical properties of the alloy itself should be considered as an important factor.

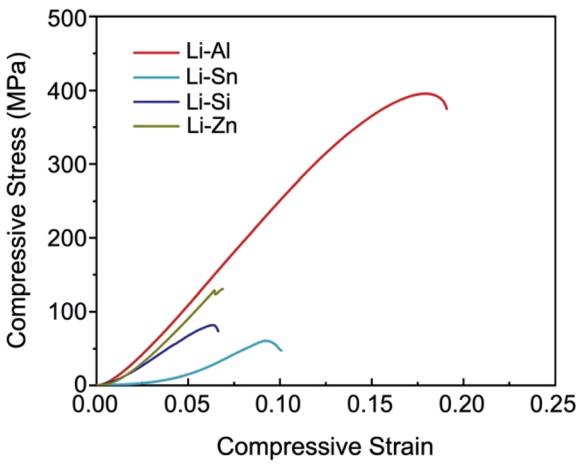

Fig. 6 Stress–strain curves of the Li alloys during a compression test. The compression rate is 0.1 mm min^{-1}.

Even though Li–Al alloy can be regarded as an ideal anode that enables the stable cycling of Li without shorting at high current density and high areal capacity in both symmetric cells and solid-state lithium–sulfur cells, the medium lithium content, and the introduction of SE to form 3D composite electrodes will inevitably increase the electrode weight, thereby reducing the energy density of the battery. It should be noted that the lithium content in the alloy will also affect the electrochemical performance. Increasing the lithium content may promote dendrite formation while decreasing the lithium content may lead to void formation at the interfaces during stripping. On the other hand, one of the advantages of solidifying batteries is the enhanced kinetics due to the elimination of concentration gradients in liquid electrolytes as well as the high volumetric lithium concentrations in SEs.[19,61,62] However, SSBs with extremely high power have only been achieved with $Li_4Ti_5O_{12}$ as the anode which limits the overall energy density of the battery.[63] In this regard, developing alloy composite anodes may greatly increase the energy density of high-power SSBs due to the higher capacity and lower voltage than $Li_4Ti_5O_{12}$ anode. Future efforts are needed to optimize the compositions, particle size, weight ratio, and N/P ratio of Li–Al composite anodes to improve electrochemical performance. Another implication of

this work is the utilization of Li–Al alloy as 3D hosts for Li metal anodes.

3 Conclusion

This work evaluated the dendrite suppression capability of SSBs with common Li alloys, including Li–Zn, Li–Si, Li–Sn, and Li–Al. The results show that soft shorting can still occur in SSBs using some alloys as anodes, even if the alloy with a medium lithium content was used in the 3D alloy/SE composite electrode. It is also reported that the Li–Al alloy performed much better than the other alloys in dendrite suppression. No soft shorting was observed at a high current density of 40 mA cm^{-2} and a capacity of 3 mA h cm^{-2} for Li–Al|LPSCl|Li–Al symmetric cells. The excellent dendrite suppression capability of Li–Al alloy was also demonstrated in SSBs using sulfur cathodes with high areal loading (10 mA h cm^{-2}). The Li–Al|LPSCl|S full batteries can stably cycle at high rates up to 1C and deliver the largest capacity among all relevant reports, considering the N/P ratio applied for our Li–Al|LPSCl|S full batteries. The superior performance of Li–Al alloy also implies that the mechanical properties of the alloys need to be considered to prevent dendrite formation on alloy anodes in future research. This work highlights the importance of studying Li dendrite behaviors and the related failure mechanisms of alloy anodes for the future development of high-rate and high-areal-capacity SSBs.

4 Experimental

4.1 Materials synthesis

Li alloys with the compositions of $Li_{0.5}Zn$, Li_2Si, Li_7Sn_3, and Li_4Al_6 were prepared by the direct alloying method. Li and alloying components (≥99.9%, Alfa Aesar) with specific stoichiometric ratios were placed into molybdenum crucibles and heated in a furnace located inside the glovebox. The melt was fully stirred before casting on a stainless-steel plate. After solidification, alloy ingots were pulverized in an agate mortar. The alloy powders were sieved, resulting in similar particle sizes of 50 μm. The sieved alloy powders were mixed with LPSCl SE in glass vials by using a vortex mixer (VX-200, VWR) for at least 15 minutes to ensure uniform powder distribution. The volume fraction of the alloy powders in the alloy composites was fixed at 50%. LPSCl was prepared by solid-state synthesis. Li_2S, P_2S_5, and LiCl powders were weighed in the molar ratio of 1.9 : 0.5 : 1.6. The reactants were ball-milled at 500 rpm for 15 hours with a ball-to-material ratio of 40 : 1. The mixture was pressed into pellets and then sealed into a quartz tube. The quartz tube was annealed at 510 °C for 2 hours.

$Li_{0.5}In$/LPSCl composites were prepared as counter electrodes by mixing the stoichiometric amounts of stabilized Li metal powders (FMC) and indium powders (99.99%, Sigma Aldrich) for 30 minutes. LPSCl was then added to the Li–In powder mixture and mixed for 15 minutes. The weight ratio of the Li–In mixture to LPSCl was 4 : 1. To prepare sulfur composite cathodes, sulfur (99.998%, Sigma Aldrich) and vapor-grown carbon fiber (VGCF) were ball-milled in a stainless-steel jar at 380 rpm for 10 hours. After ball-milling, the sulfur/VGCF mixture was mixed with LPSCl and ball-milled at 380 rpm for 40 hours. The weight ratio of sulfur, VGCF, and LPSCl in the cathode composite is 3 : 1 : 6.

4.2 Materials characterization

Alloy powders and LPSCl SE were characterized by X-ray diffraction (XRD) using a PanAlytical X'Pert Diffractometer with a copper irradiation source (Cu $K\alpha = 0.15406$ nm). The morphology of alloy powders was observed by the Zeiss Supra 55 field emission scanning electron microscope (FESEM) with a Schottky thermal field emission source.

4.3 Electrochemical measurement

The symmetrical cells were prepared by sandwiching LPSCl SE between two layers of alloy composites. 120 mg LPSCl was cold-pressed in the PEEK tube with a diameter of 10 mm at 350 MPa. Excessive amounts of Li alloy composites (total capacity: ~30 mA h for each alloy composite anode) were added to both sides of the compacted LPSCl and then pressed at 250 MPa to make symmetrical batteries. The same procedures were also used to prepare the Li–Al|LPSCl|Li–In cells but with a limited amount of Li–Al composites. The electrochemical performance of all the cells was tested using Arbin BT 2000 Battery Tester. The testing capacity was 3 mA h cm^{-2}. The current density was gradually increased to 40 mA cm^{-2}, and batteries were tested for one cycle at each current density. The cells were tested under a stacking pressure of 70 MPa at room temperature.

To prepare solid-state lithium–sulfur batteries, 120 mg LPSCl was cold-pressed in the PEEK tube with a diameter of 10 mm at 350 MPa, 15.63 mg sulfur composite cathode (theoretical areal capacity: 10 mA h cm^{-2}), and 94.94 mg Li–Al composite anode (theoretical areal capacity: 34 mA h cm^{-2}) were added and pressed at 250 MPa. The rate performance of Li–Al|LPSCl|S batteries was tested within a voltage range of 0.6–2.6 V (*vs.* Li–Al alloy anode) with increasing current densities of 0.5, 1.0, 2.0, 4.0, 6.0, 8.0, and 10.0 mA cm^{-2}. The cycling performance of Li–Al|LPSCl|S batteries was tested within a voltage range of 0.6–2.6 V (*vs.* Li–Al alloy anode) at a current density of 2 mA cm^{-2}. The batteries were tested under a stacking pressure of 70 MPa at either 60 °C or room temperature.

4.4 Compression test

The alloy powders were pressed into cylinders with a diameter of 8 mm and a height of ~2 mm. The pressing stress is 1000 MPa. Some alloys, such as Li–Si, cannot be pressed to a height of more than 2 mm, therefore, all the alloy specimens were pressed to ~2 mm high and thus the compression properties can be evaluated with the same dimensions. The alloy cylinders were sealed inside the plastic bags and tested by the Instron 4204 machine. The compression rate is 0.1 mm min^{-1}.

Author contributions

Y. Huang conducted the experiments, analyzed the data, and wrote the manuscript. B. Shao assisted in the experiments. All

authors discussed the results. F. Han conceived the idea and supervised the project.

Conflicts of interest

There are no conflicts to declare.

Acknowledgements

F. Han acknowledges support from the Priti and Mukesh Chatter Career Development Chair Professorship at the Rensselaer Polytechnic Institute.

References

1 J. Janek and W. G. Zeier, *Nat. Energy*, 2016, **1**, 1–4.
2 P. Albertus, V. Anandan, C. M. Ban, N. Balsara, I. Belharouak, J. Buettner-Garrett, Z. H. Chen, C. Daniel, M. Doeff, N. J. Dudney, B. Dunn, S. J. Harris, S. Herle, E. Herbert, S. Kalnaus, J. A. Libera, D. P. Lu, S. Martin, B. D. McCloskey, M. T. McDowell, Y. S. Meng, J. Nanda, J. Sakamoto, E. C. Self, S. Tepavcevic, E. Wachsman, C. S. Wang, A. S. Westover, J. Xiao and T. Yersak, *ACS Energy Lett.*, 2021, **6**, 1399–1404.
3 M. Nagao, A. Hayashi, M. Tatsumisago, T. Kanetsuku, T. Tsuda and S. Kuwabata, *Phys. Chem. Chem. Phys.*, 2013, **15**, 18600–18606.
4 S. Wenzel, D. A. Weber, T. Leichtweiss, M. R. Busche, J. Sann and J. Janek, *Solid State Ionics*, 2016, **286**, 24–33.
5 T. K. Schwietert, V. A. Arszelewska, C. Wang, C. Yu, A. Vasileiadis, N. J. J. de Klerk, J. Hageman, T. Hupfer, I. Kerkamm, Y. L. Xu, E. van der Maas, E. M. Kelder, S. Ganapathy and M. Wagemaker, *Nat. Mater.*, 2020, **19**, 428–435.
6 Y. Y. Ren, Y. Shen, Y. H. Lin and C. W. Nan, *Electrochem. Commun.*, 2015, **57**, 27–30.
7 R. Garcia-Mendez, F. Mizuno, R. G. Zhang, T. S. Arthur and J. Sakamoto, *Electrochim. Acta*, 2017, **237**, 144–151.
8 L. Porz, T. Swamy, B. W. Sheldon, D. Rettenwander, T. Frömling, H. L. Thaman, S. Berendts, R. Uecker, W. C. Carter and Y. M. Chiang, *Adv. Energy Mater.*, 2017, **7**, 1701003.
9 F. D. Han, A. S. Westover, J. Yue, X. L. Fan, F. Wang, M. F. Chi, D. N. Leonard, N. Dudney, H. Wang and C. S. Wang, *Nat. Energy*, 2019, **4**, 187–196.
10 T. Krauskopf, F. H. Richter, W. G. Zeier and J. Janek, *Chem. Rev.*, 2020, **120**, 7745–7794.
11 T. Krauskopf, B. Mogwitz, C. Rosenbach, W. G. Zeier and J. Janek, *Adv. Energy Mater.*, 2019, **9**, 1902568.
12 J. Kasemchainan, S. Zekoll, D. S. Jolly, Z. Y. Ning, G. O. Hartley, J. Marrow and P. G. Bruce, *Nat. Mater.*, 2019, **18**, 1105–1111.
13 J. A. Lewis, F. J. Q. Cortes, Y. Liu, J. C. Miers, A. Verma, B. S. Vishnugopi, J. Tippens, D. Prakash, T. S. Marchese, S. Y. Han, C. Lee, P. P. Shetty, H. W. Lee, P. Shevchenko, F. D. Carlo, C. Saldana, P. P. Mukherjee and M. T. McDowell, *Nat. Mater.*, 2021, **20**, 503–510.
14 S. F. Wang, H. H. Xu, W. D. Li, A. Dolocan and A. Manthiram, *J. Am. Chem. Soc.*, 2018, **140**, 250–257.
15 M. J. Wang, R. Choudhury and J. Sakamoto, *Joule*, 2019, **3**, 2165–2178.
16 T. Krauskopf, B. Mogwitz, H. Hartmann, D. K. Singh, W. G. Zeier and J. Janek, *Adv. Energy Mater.*, 2020, **10**, 2000945.
17 M. Chiku, W. Tsujiwaki, E. Higuchi and H. Inoue, *Electrochemistry*, 2012, **80**, 740–742.
18 K. B. Hatzell, X. C. Chen, C. L. Cobb, N. P. Dasgupta, M. B. Dixit, L. E. Marbella, M. T. McDowell, P. P. Mukherjee, A. Verma, V. Viswanathan, A. S. Westover and W. G. Zeier, *ACS Energy Lett.*, 2020, **5**, 922–934.
19 T. Krauskopf, H. Hartmann, W. G. Zeier and J. Janek, *ACS Appl. Mater. Interfaces*, 2019, **11**, 14463–14477.
20 W. Luo, Y. H. Gong, Y. Z. Zhu, Y. J. Li, Y. G. Yao, Y. Zhang, K. Fu, G. Pastel, C. F. Lin, Y. F. Mo, E. D. Wachsman and L. B. Hu, *Adv. Mater.*, 2017, **29**, 1606042.
21 Y. Lu, X. Huang, Y. D. Ruan, Q. S. Wang, R. Kun, J. H. Yang and Z. Y. Wen, *J. Mater. Chem. A*, 2018, **6**, 18853–18858.
22 K. Fu, Y. H. Gong, B. Y. Liu, Y. Z. Zhu, S. M. Xu, Y. G. Yao, W. Luo, C. W. Wang, S. D. Lacey, J. Q. Dai, Y. N. Chen, Y. F. Mo, E. D. Wachsman and L. B. Hu, *Sci. Adv.*, 2017, **3**, e1601659.
23 M. H. He, Z. H. Cui, C. Chen, Y. Q. Li and X. X. Guo, *J. Mater. Chem. A*, 2018, **6**, 11463–11470.
24 C. L. Tsai, V. Roddatis, C. V. Chandran, Q. L. Ma, S. Uhlenbruck, M. Bram, P. Heitjans and O. Guillon, *ACS Appl. Mater. Interfaces*, 2016, **8**, 10617–10626.
25 N. J. Taylor, S. Stangeland-Molo, C. G. Haslam, A. Sharafi, T. Thompson, M. Wang, R. Garcia-Mendez and J. Sakamoto, *J. Power Sources*, 2018, **396**, 314–318.
26 W. Luo, Y. H. Gong, Y. Z. Zhu, K. K. Fu, J. Q. Dai, S. D. Lacey, C. W. Wang, B. Y. Liu, X. G. Han, Y. F. Mo, E. D. Wachsman and L. B. Hu, *J. Am. Chem. Soc.*, 2016, **138**, 12258–12262.
27 K. Fu, Y. H. Gong, Z. Z. Fu, H. Xie, Y. G. Yao, B. Y. Liu, M. Carter, E. D. Wachsman and L. B. Hu, *Angew. Chem., Int. Ed.*, 2017, **56**, 14942–14947.
28 Y.-G. Lee, S. Fujiki, C. Jung, N. Suzuki, N. Yashiro, R. Omoda, D.-S. Ko, T. Shiratsuchi, T. Sugimoto, S. Ryu, J. H. Ku, T. Watanabe, Y. Park, Y. Aihara, D. Im and I. T. Han, *Nat. Energy*, 2020, **5**, 299–308.
29 C. P. Yang, H. Xie, W. W. Ping, K. Fu, B. Y. Liu, J. C. Rao, J. Q. Dai, C. W. Wang, G. Pastel and L. B. Hu, *Adv. Mater.*, 2019, **31**, 1804815.
30 T. A. Yersak, S.-B. Son, J. S. Cho, S.-S. Suh, Y.-U. Kim, J.-T. Moon, K. H. Oh and S.-H. Lee, *J. Electrochem. Soc.*, 2013, **160**, A1497–A1501.
31 R. B. Cervera, N. Suzuki, T. Ohnishi, M. Osada, K. Mitsuishi, T. Kambara and K. Takada, *Energy Environ. Sci.*, 2014, **7**, 662–666.
32 H. W. Park, J.-H. Song, H. Choi, J. S. Jin and H.-T. Lim, *Jpn. J. Appl. Phys.*, 2014, **53**, 08NK02.
33 J. M. Whiteley, J. W. Kim, C. S. Kang, J. S. Cho, K. H. Oh and S.-H. Lee, *J. Electrochem. Soc.*, 2015, **162**, A711–A715.
34 M. Yamamoto, Y. Terauchi, A. Sakuda and M. Takahashi, *J. Power Sources*, 2018, **402**, 506–512.

35 A. L. Santhosha, L. Medenbach, J. R. Buchheim and P. Adelhelm, *Batter. Supercaps*, 2019, **2**, 524–529.
36 S. Cangaz, F. Hippauf, F. S. Reuter, S. Doerfler, T. Abendroth, H. Althues and S. Kaskel, *Adv. Energy Mater.*, 2020, **10**, 2001320.
37 R. Miyazaki, *Front. Energy Res.*, 2020, **8**, 171.
38 J. A. S. Oh, J. G. Sun, M. Goh, B. Chua, K. Y. Zeng and L. Lu, *Adv. Energy Mater.*, 2021, **11**, 2101228.
39 J. Y. Kim, S. Jung, S. H. Kang, J. Park, M. J. Lee, D. Jin, D. O. Shin, Y. G. Lee and Y. M. Lee, *Adv. Energy Mater.*, 2022, **12**, 2103108.
40 M. N. Obrovac and V. L. Chevrier, *Chem. Rev.*, 2014, **114**, 11444–11502.
41 D. H. S. Tan, Y.-T. Chen, H. D. Yang, W. Bao, B. Sreenarayanan, J.-M. Doux, W. K. Li, B. Y. Lu, S.-Y. Ham, B. Sayahpour, J. Scharf, E. A. Wu, G. Deysher, H. E. Han, H. J. Hah, H. Jeong, J. B. Lee, Z. Chen and Y. S. Meng, *Science*, 2021, **373**, 1494–1499.
42 R. Kanno, M. Murayama, T. Inada, T. Kobayashi, K. Sakamoto, N. Sonoyama, A. Yamada and S. Kondo, *Electrochem. Solid-State Lett.*, 2004, **7**, A455–A458.
43 M. Sakuma, K. Suzuki, M. Hirayama and R. Kanno, *Solid State Ionics*, 2016, **285**, 101–105.
44 C. Hänsel, B. Singh, D. Kiwic, P. Canepa and D. Kundu, *Chem. Mater.*, 2021, **33**, 6029–6040.
45 H. Kitaura, A. Hayashi, K. Tadanaga and M. Tatsumisago, *J. Power Sources*, 2009, **189**, 145–148.
46 M. Garreau, J. Thevenin and M. Fekir, *J. Power Sources*, 1983, **9**, 235–238.
47 J. M. Doux, H. Nguyen, D. H. S. Tan, A. Banerjee, X. F. Wang, E. A. Wu, C. Jo, H. D. Yang and Y. S. Meng, *Adv. Energy Mater.*, 2020, **10**, 1903253.
48 Y. Huang, B. Shao and F. Han, *Curr. Opin. Electrochem.*, 2022, **33**, 100933.
49 H. Kim, B. Park, H.-J. Sohn and T. Kang, *J. Power Sources*, 2000, **90**, 59–63.
50 Y. D. Ruan, Y. Lu, Y. P. Li, C. J. Zheng, J. M. Su, J. Jin, T. P. Xiu, Z. Song, M. E. Badding and Z. Y. Wen, *Adv. Funct. Mater.*, 2021, **31**, 2007815.
51 C. Z. Sun, Y. P. Li, J. Jin, J. H. Yang and Z. Y. Wen, *J. Mater. Chem. A*, 2019, **7**, 7752–7759.
52 J. Q. Wang, P. King and R. A. Huggins, *Solid State Ionics*, 1986, **20**, 185–189.
53 J. Q. Wang, I. D. Raistrick and R. A. Huggins, *J. Electrochem. Soc.*, 1986, **133**, 457–460.
54 B. M. L. Rao, R. W. Francis and H. A. Christopher, *J. Electrochem. Soc.*, 1977, **124**, 1490–1492.
55 K. Yan, Z. D. Lu, H.-W. Lee, F. Xiong, P.-C. Hsu, Y. Z. Li, J. Zhao, S. Chu and Y. Cui, *Nat. Energy*, 2016, **1**, 1–8.
56 P. Albertus, S. Babinec, S. Litzelman and A. Newman, *Nat. Energy*, 2018, **3**, 16–21.
57 X. Xing, Y. J. Li, S. Wang, H. D. Liu, Z. H. Wu, S. C. Yu, J. Holoubek, H. Y. Zhou and P. Liu, *ACS Energy Lett.*, 2021, **6**, 1831–1838.
58 J. R. Owen, W. C. Maskell, B. C. H. Steele, T. S. Nielsen and O. T. Sörensen, *Solid State Ionics*, 1984, **13**, 329–334.
59 R. A. Huggins, *J. Power Sources*, 1999, **81**, 13–19.
60 F. P. Beer, E. R. Johnston, J. T. DeWolf and D. F. Mazurek, *Mechanics of Materials*, MeGraw-Hill Education Ltd, New York, 7th edn, 2015.
61 J. Xiao, *Science*, 2019, **366**, 426–427.
62 J. Liu, Z. N. Bao, Y. Cui, E. J. Dufek, J. B. Goodenough, P. Khalifah, Q. Y. Li, B. Y. Liaw, P. Liu, A. Manthiram, Y. S. Meng, V. R. Subramanian, M. F. Toney, V. V. Viswanathan, M. Stanley Whittingham, J. Xiao, W. Xu, J. H. Yang, X. Q. Yang and J. G. Zhang, *Nat. Energy*, 2019, **4**, 180–186.
63 Y. Kato, S. Hori, T. Saito, K. Suzuki, M. Hirayama, A. Mitsui, M. Yonemura, H. Iba and R. Kanno, *Nat. Energy*, 2016, **1**, 1–7.